



# Linked influences on slab stagnation: Interplay between lower mantle viscosity structure, phase transitions, and plate coupling

Hana Čížková<sup>a</sup>, Craig R. Bina<sup>b</sup>

<sup>a</sup> Charles University, Faculty of Mathematics and Physics, Department of Geophysics, Prague, Czech Republic

<sup>b</sup> Northwestern University, Department of Earth and Planetary Sciences, Evanston, IL, USA

## ARTICLE INFO

### Article history:

Received 26 June 2018

Received in revised form 22 November 2018

Accepted 22 December 2018

Available online 11 January 2019

Editor: B. Buffett

### Keywords:

subduction dynamics

upper-lower mantle rheological transition

slab stagnation

## ABSTRACT

An endothermic phase transition in mantle material at 660-km depth constitutes a barrier that in most cases prevents the direct penetration of subducted slabs. Seismic tomography shows that subducted material is in many subduction zones trapped at the bottom of the transition zone, just above the 660-km phase boundary. Recent tomographic models however also report subducted material that penetrates to the shallow lower mantle, and there it is observed to flatten at about 1000-km depth. Models of slab dynamics that generally assume sharp rheological transition at 660-km depth, however, mostly predict slab stagnation at the bottom of the transition zone. Multiple lines of evidence, including recent experiments, indicate that viscosity may gradually increase in the uppermost ~300 km of the lower mantle, rather than simply changing abruptly at the upper-lower mantle boundary. Here we present the results of a modeling study focused on the effects of rheological transition between upper and lower mantle material on slab deformation and stagnation. We test the effects of smoothing the viscosity increase over 300 km and shifting it to a depth of 1000 km or even deeper. We show that slab ability to penetrate to the lower mantle is mainly controlled by the trench migration rate, which in turn is affected by crustal viscosity. Coupling between the subducting and overriding plates thus plays a key role in controlling slab penetration to the lower mantle and stagnation in the deep transition zone or shallow lower mantle. Models with strong crust and consequently negligible rollback display penetration to the lower mantle without much hindrance and no stagnation above or below the 660-km interface, regardless of viscosity stratification in the shallow lower mantle. Models with weak crust are characterized by fast rollback, and penetration is very limited as slabs buckle horizontally and flatten above the 660-km boundary. Most interesting from the point of view of shallow lower mantle stagnation are models with intermediate crustal viscosity. Here rollback is efficient, though slower than in weak-crust cases. Horizontally lying slab segments are trapped in the transition zone if the sharp viscosity increase occurs at 660 km, but shifting the viscosity increase to 1000 km depth allows for efficient sinking of the flat-lying part and results in temporary stagnation below the upper-lower mantle boundary at about 1000 km depth.

© 2019 Elsevier B.V. All rights reserved.

## 1. Introduction

It has long been known from dynamical modeling of subduction that slab deflection at the base of the mantle transition zone may arise from combinations of variations in density, viscosity, or phase-transition Clapeyron slopes (Christensen and Yuen, 1984; Christensen, 2001). Furthermore, seismological observations have long indicated that, while some subducting slabs penetrate into the upper mantle, others appear to deflect and stagnate at depths of ~660 km (Fukao et al., 2009). More recent observa-

tions (Fukao and Obayashi, 2013) have confirmed that some such deflected slabs appear to stagnate at greater depths of ~1000 km (e.g., Java, Tonga-Kermadec, southern Peru, Central America, northern Kuriles).

Driving forces for slab stagnation likely include a combination of surface tractions imposed by viscosity increase at depth and buoyant body forces arising from thermally shifted endothermic phase transition, such as the ringwoodite disproportionation reaction (Bina et al., 2001; Torii and Yoshioka, 2007; Billen, 2008), perhaps augmented by additional buoyant body forces due to metastable persistence of low-density mineral phases at lower temperatures (Tetzlaff and Schmeling, 2000; Agrusta et al., 2014; King et al., 2015). While petrological body forces alone likely

E-mail address: Hana.Cizkova@mff.cuni.cz (H. Čížková).

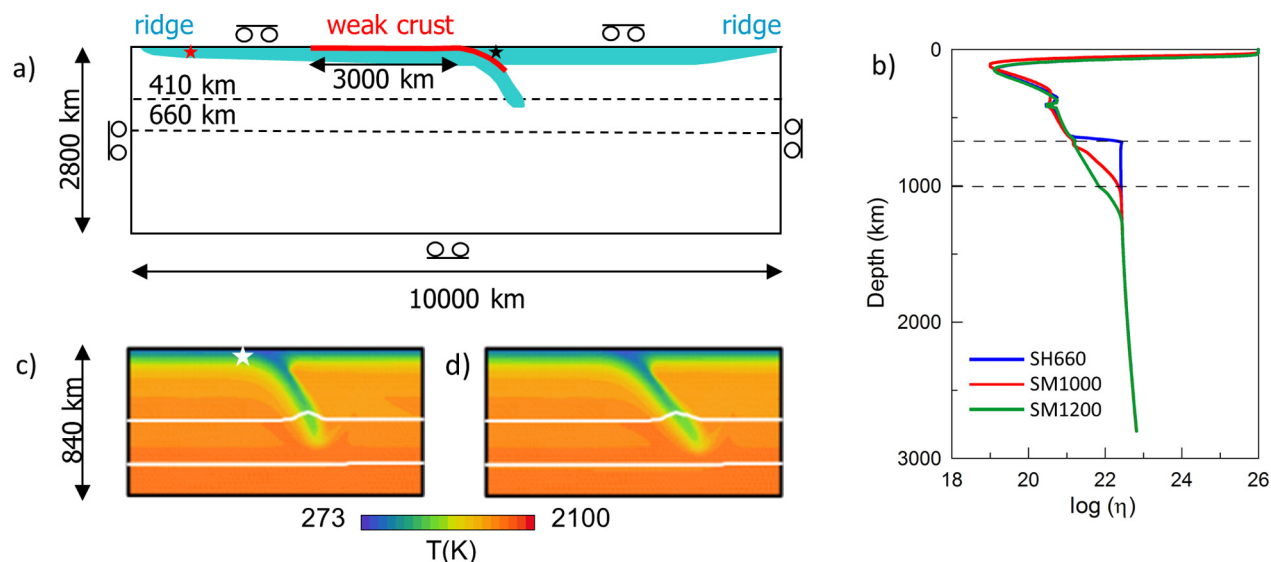


**Fig. 1.** a) Model domain, 10000 km wide and 2800 km deep. Dashed lines mark the major phase transition boundaries. Subducting and overriding plates are given in blue; red indicates 10-km thick weak crust separating the plates. b) Viscosity profiles used in this study. Models SH660 (blue) with a sharp viscosity increase at 660-km depth, SM1000 (red) with a smooth increase reaching the lower mantle viscosity at 1000-km depth and SM1200 (green) reaching the lower mantle viscosity at 1200-km depth. Profiles show vertical cross-section of viscosity taken at initial snapshot at a distance 3000 km to the left of the trench and they thus represent the background mantle viscosity. c) Initial temperature distribution (at  $t = 0$  Myr) *Ini1* zoomed around slab tip. White lines mark the position of the major phase transitions at 410 km and 660 km depths. White asterisk marks the position of the tracer used to monitor slab penetration depth. d) The same as c), but for model *Ini2* that differs from *Ini1* by the dip angle of the slab. Temperature anomaly of the slab with respect to the ambient mantle in both cases *Ini1* and *Ini2* is comparable. (For interpretation of the figure(s), the reader is referred to the web version of this article.)

bracket equilibrium stagnation depths in a region near  $\sim 660$  km (Bina and Kawakatsu, 2010), the prospect of complex viscosity structures potentially allows for greater variation in stagnation depths.

Studies of geophysical observables arising from Earth's response to surface and internal loading have long indicated an increase in viscosity between the upper and lower mantle, but they have not uniquely prescribed the precise form nor depth range of such increase (Čížková et al., 1996; Mitrova and Forte, 1997). Viscosity structure has most commonly been modeled as a sharp increase near 660 km depth, but views of viscosity structure within and below the mantle transition zone continue to evolve (King, 2016). Recent geoid analyses suggest either a mid-mantle viscosity increase at  $\sim 800$ – $1200$  km (Rudolph et al., 2015) or the absence of a mid-mantle viscosity increase (Liu and Zhong, 2016), depending upon the context of seismic tomographic constraints on density structure, while seismological studies of plume structures support higher mantle viscosities below  $\sim 1000$  km (French and Romanowicz, 2015).

The disproportionation of ringwoodite to an assemblage of ferropericlase (magnesiowüstite) and intrinsically strong (Yamazaki and Karato, 2001; Chen et al., 2002) bridgmanite (ferromagnesian silicate perovskite) is typically invoked as an underlying petrological rationale for locating a viscosity increase at  $\sim 660$  km depth. However, such petrological reasoning can be extended in support of an ongoing, more gradual, increase in viscosity below this depth (Faccenda and Dal Zilio, 2017). For example, the sharp ringwoodite disproportionation reaction is succeeded by a more gradual transformation of garnet-majorite solid solution to bridgmanite (Wood and Rubie, 1996) to depths of  $\sim 800$  km, further increasing the stable fraction of strong bridgmanite. Furthermore, the low solubility of OH in bridgmanite (Bolfan-Casanova et al., 2003) suggests progressive dehydration of the shallow lower mantle, and consequent further strengthening, as this phase grows more abundant. Other mechanisms proposed for contributing to viscosity increase at even greater depths include a potential pressure-induced viscosity change in ferropericlase (Marquardt and Miyagi, 2015) and possible compositional variations (Ballmer et al., 2015).

Here we use numerical models of subduction dynamics to investigate the roles of such fundamental factors as crustal strength, transition-zone Clapeyron slopes, and lower-mantle viscosity profiles in governing slab deformation and stagnation.

## 2. Methods

Our model of subduction dynamics is based on the solution of governing equations in the extended Boussinesq approximation without internal heating (Čížková et al., 2007), using a finite-element method implemented in the SEPRAN package (Segal and Praagman, 2005). A 2D Cartesian model domain (Fig. 1a) represents part of the mantle 10,000 km wide and 2800 km deep. All boundaries are considered impermeable free-slip. The subducting plate extends from the ridge in the upper left corner to the trench initially located at 6000 km distance from the ridge. Another ridge positioned in the upper right corner of the box ensures the horizontal mobility of the overriding plate (Čížková and Bina, 2013). The initial temperature distribution in the subducting and overriding plates follows a half-space model. The age of the plate at the trench is 100 Myr in most models, but we also test the effects of younger (50 Myr) and older (150 Myr) plates. Below the plates an adiabatic temperature profile is prescribed with a potential temperature of 1573 K. In order to avoid complications with plumes that would originate from the bottom thermal boundary layer, our model domain ends 100 km above the core–mantle boundary. The subducting plate has a tip initially reaching the depth of 500 km (Fig. 1c). This tip is produced in a kinematically driven preliminary run where a constant velocity of 5 cm/yr is prescribed at the surface of the subducting plate, and the end of this kinematic initialization represents  $t = 0$  for all subsequent dynamical simulations.

Major mantle phase transitions at 410-km and 660-km depths are included in the model (both buoyancy and latent heat effects) using a phase function with harmonic parameterization (Čížková et al., 2007). The Clapeyron slope of the exothermic olivine-wadsleyite transition is set at 2 MPa/K. In the case of the endothermic bridgmanite-forming transition at 660 km, which is presum-

**Table 1**  
Symbols and model parameters.

Symbol	Meaning	Value	Units
Upper mantle and transition zone rheology			
$A_{\text{diff}}$	Pre-exponential parameter of diffusion creep <sup>a</sup>	$1 \times 10^{-9}$	$\text{Pa}^{-1} \text{s}^{-1}$
$A_{\text{disl}}$	Pre-exponential parameter of dislocation creep <sup>a</sup>	$3.1 \times 10^{-17}$	$\text{Pa}^{-n} \text{s}^{-1}$
$E_{\text{diff}}$	Activation energy of diffusion creep <sup>a</sup>	$3.35 \times 10^5$	$\text{J mol}^{-1}$
$E_{\text{disl}}$	Activation energy of dislocation creep <sup>a</sup>	$4.8 \times 10^5$	$\text{J mol}^{-1}$
$V_{\text{diff}}$	Activation volume of diffusion creep <sup>a</sup>	$4.0 \times 10^{-6}$	$\text{m}^3 \text{mol}^{-1}$
$V_{\text{disl}}$	Activation volume of dislocation creep <sup>a</sup>	$11 \times 10^{-6}$	$\text{m}^3 \text{mol}^{-1}$
$N$	Power-law exponent	3.5	–
$\eta_{\text{crust}}$	Viscosity of crust	$10^{20}, 5 \times 10^{20}, 10^{21}$	$\text{Pa s}$
$\tau_y$	Yield stress	$5 \times 10^8$	$\text{Pa}$
$e_y$	Reference strainrate	$10^{-15}$	$\text{s}^{-1}$
$n_y$	Stress limiter exponent	10	–
$P$	Hydrostatic pressure	–	$\text{Pa}$
$R$	Gas constant	8.314	$\text{J K}^{-1} \text{mol}^{-1}$
$T$	Temperature	–	$\text{K}$
$E$	Second invariant of the strainrate	–	$\text{s}^{-1}$
Lower mantle rheology			
$A_{\text{diff}}$	Pre-exponential parameter of diffusion creep	$1.3 \times 10^{-16}$	$\text{Pa}^{-1} \text{s}^{-1}$
$E_{\text{diff}}$	Activation energy of diffusion creep <sup>b</sup>	$2 \times 10^5$	$\text{J mol}^{-1}$
$V_{\text{diff}}$	Activation volume of diffusion creep <sup>b</sup>	$1.1 \times 10^{-6}$	$\text{m}^3 \text{mol}^{-1}$
Other model parameters			
$\kappa$	Diffusivity	$10^{-6}$	$\text{m}^2 \text{s}^{-1}$
$G$	Gravitational acceleration	9.8	$\text{m s}^{-2}$
$\rho_0$	Reference density	3416	$\text{kg m}^{-3}$
$c_p$	Specific heat	1250	$\text{J kg}^{-1} \text{K}^{-1}$
$\alpha_0$	Surface thermal expansivity	$3 \times 10^{-5}$	$\text{K}^{-1}$
$\gamma_{410}$	Clapeyron slope 410 km phase transition <sup>c</sup>	$2 \times 10^6$	$\text{Pa K}^{-1}$
$\gamma_{660}$	Clapeyron slope 660 km phase transition <sup>c</sup>	$0, -1.5 \times 10^6, -2.5 \times 10^6$	$\text{Pa K}^{-1}$
$\delta\rho_{410}$	Density contrast 410 km phase transition <sup>d</sup>	273	$\text{kg m}^{-3}$
$\delta\rho_{660}$	Density contrast 660 km phase transition <sup>d</sup>	341	$\text{kg m}^{-3}$

<sup>a</sup> Parameters of wet olivine based on Hirth and Kohlstedt (2003).

<sup>b</sup> Čížková et al. (2012).

<sup>c</sup> Bina and Helffrich (1994).

<sup>d</sup> Steinbach and Yuen (1995).

ably more important in controlling the penetration and stagnation of the slab, we test two values of Clapeyron slope:  $-2.5 \text{ MPa/K}$  (hereafter referred to as “regular” phase transition model) and a weaker  $-1.5 \text{ MPa/K}$ . We also execute a model without phase transitions for reference.

Rheology of the upper mantle follows a composite model (van den Berg et al., 1993) that combines diffusion creep, dislocation creep and power-law stress limiter (van Hunen et al., 2002) with the activation parameters based on wet olivine rheology (Hirth and Kohlstedt, 2003). The lower mantle is assumed to deform via diffusion creep with activation parameters based on slab sinking speed analysis (Čížková et al., 2012). The rheological transition between upper and lower mantle is one of the key parameters in our analysis. Numerical models traditionally assume that the phase boundary at 660 km depth is associated with a stepwise increase of viscosity. Recent reanalysis of long-wavelength geoid (Rudolph et al., 2015), however, detects an increase of viscosity at 800–1200 km. Also, deformation experiments on ferropericlase (Marquardt and Miyagi, 2015) suggest that the uppermost part of the lower mantle may actually be relatively weak, with viscosity gradually increasing and reaching its maximum at about 1000 km depth.

We therefore focus on the effects of the upper-lower mantle viscosity transition here. In the reference model we consider it to occur at 660 km depth, and in agreement with sinking-speed analysis (Čížková et al., 2012) we associate it with a sharp stepwise increase of viscosity by a factor of 19 (Fig. 1b, blue line, models further abbreviated as SH660). This reference profile is then compared with two other models: 1) a viscosity transition smoothed over 300 km such that it attains the maximum lower mantle value at 1000 km (Fig. 1b, red line, abbreviated SM1000) and 2) the viscosity interface shifted yet deeper, to a depth of 1200 km (Fig. 1b, green line, SM1200). Smooth viscosity transition below

660-km depth is obtained as a weighted average of the viscosities of the upper mantle material and lower mantle material. The weight is the volume fraction of lower mantle material, which is harmonically increasing from 0 to 1 between depths of 660 km and 1000 km in case of model SM1000 (and between depths of 660 km and 1200 km in case of model SM1200).

On top of the subducting plate a weak crust-like layer is positioned (Běhounková and Čížková, 2008). It is 10 km thick, and its low viscosity effectively decouples the subducting and the over-riding plates and lubricates their contact. The constant viscosity of this decoupling layer is one of the free parameters in our study, and we vary it between  $10^{20} \text{ Pa s}$  and  $10^{21} \text{ Pa s}$ . It initially stretches 3000 km to the left from the trench. After this weak crust is fully subducted, we obtain a locked-slab situation soon followed by slab break-off. Thus, we can also investigate the free sinking of the detached slab segment and evaluate how much it is affected by the developed slab morphology. No additional density contrast is associated with the crustal material. Below the depth of 200 km, where it is no longer needed to decouple the plates, it is replaced by mantle material.

Our assumed thermal expansivity decreases with depth from  $3 \times 10^{-5} \text{ K}^{-1}$  at the surface to  $1 \times 10^{-5} \text{ K}^{-1}$  at a depth of 2800 km (Chopelas and Boehler, 1992; Katsura et al., 2009). Thermal diffusivity is constant. For a summary of model parameters, see Table 1.

### 3. Results

#### 3.1. Effects of rheological transition between upper and lower mantle and crustal strength

Let us first illustrate slab behavior in several snapshots of temperature evolution. In Fig. 2a we show model SH660 with 100 Myr-

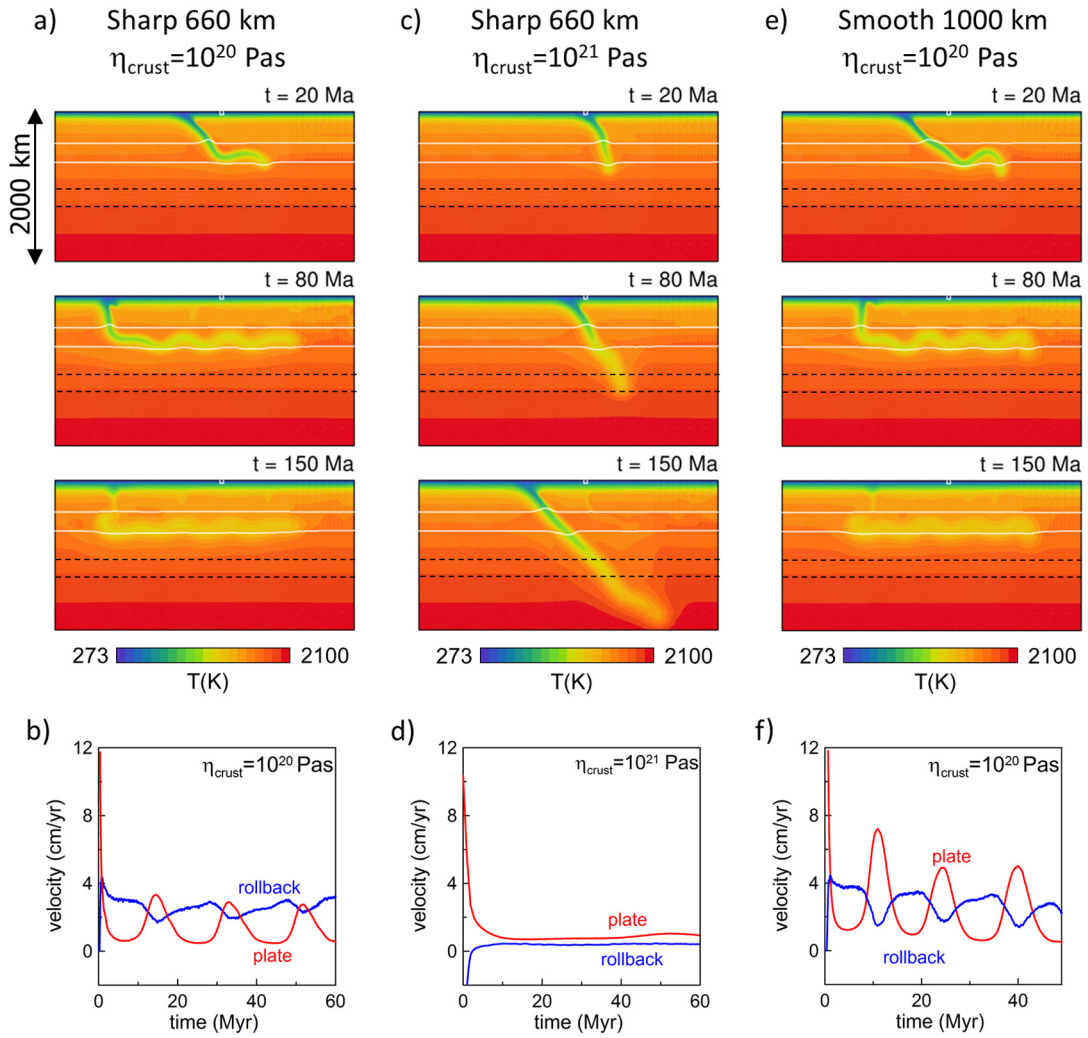


**Fig. 2.** a) Three temperature snapshots illustrating the time evolution of model SH660 with weak crust ( $\eta_{\text{crust}} = 10^{20}$  Pas). Part of the model domain 2000 km deep centered around subduction is shown. White lines mark the major phase transition boundaries; dashed black lines indicate the depths of 1000 km and 1200 km. b) Plate (red line) and rollback (blue line) velocity as a function of time for the model SH660 with weak crust. Plate velocity is evaluated using a monitor tracer originally placed 15 km deep and 1000 km to the right from the upper-left mid-ocean ridge (red asterisk in Fig. 1a). Rollback velocity is evaluated using a monitor tracer in the tip of the overriding plate (black asterisk in Fig. 1a). c), d) The same as panels a), b) but for the model SH660 with  $\eta_{\text{crust}} = 10^{21}$  Pas. e), f) The same as panels a), b) but for the model SM1000.

old plate and a weak crust. The slab slows down when approaching the bottom of the transition zone, due to the combined effects of buoyancy from an endothermic phase boundary and resistance of a more viscous lower mantle. At  $\sim 4$  Myr the tip arrives at the endothermic phase boundary. The shallowest portion of this old and cold slab, dipping at an angle under  $\sim 30^\circ$ , is not supported by the resistance of the 660-km interface far below and begins to descend vertically thus inducing trench retreat. The trench rolls back, and the slab buckles subhorizontally and remains trapped above the 660-km phase boundary. At  $\sim 140$  Myr the initially prescribed weak crust is consumed and slab break-off follows. Plate and rollback velocities (Fig. 2b) reflect the buckling. They exhibit plate velocity minima accompanied by rollback velocity maxima when slab descent is hampered by the endothermic phase boundary (and associated viscosity increase). On the other hand, when the slab weakens and forms a buckle, we observe an increase of plate velocity and rollback is temporarily delayed (Čížková and Bina, 2013). The same model (SH660, 100 Myr old plate), but now with a strong crust ( $\eta_{\text{cr}} = 10^{21}$  Pas) is shown in Fig. 2c. Stronger coupling between the subducting and overriding plates results in steeper slab dip and reduced rollback. Consequently, the slab penetrates to the lower mantle. Both plate and rollback velocities are reduced with respect to the model with weaker crust (plate ve-

locity by a factor 1.7, rollback velocity by a factor 6), as the decoupling of the subducting and overriding plates is significantly less efficient here. If we shift the viscosity interface deeper and assume a weak crust (SM1000, Fig. 2e), we observe similar behavior as in corresponding model SH660 (Fig. 2a) yet with some differences. As the viscous strength of the uppermost lower mantle now is reduced with respect to model SH660, the resistive force associated with the 660-km endothermic phase transition alone is not strong enough to prevent penetration of the slab tip. The tip thus penetrates the 660-km boundary and enters the lower mantle, but when it approaches the stiff material at 1000 km depth (at  $\sim 7$  Myr) it slows down to  $\sim 1.2$  cm/yr and a rollback period is initiated. The tip is thus observed somewhat deeper below the 660-km boundary than in case SH660 (cf. Fig. 2a and 2e at 20 Myr), but in both cases slabs roll back and stagnate above the 660-km depth. Subducting plate velocity is increased by about a factor of 1.8 with respect to the case SH660 due to the higher mobility of uppermost lower mantle, while rollback velocity is similar to the case with a sharp viscosity increase at 660 km (cf. Fig. 2f and 2b).

Having discussed these three models in more detail, let us now compare all of our experiments. They result in a broad variety of slab deformation patterns depending on several model parameters. In Fig. 3 we show results for models with a 100 Myr-old plate and



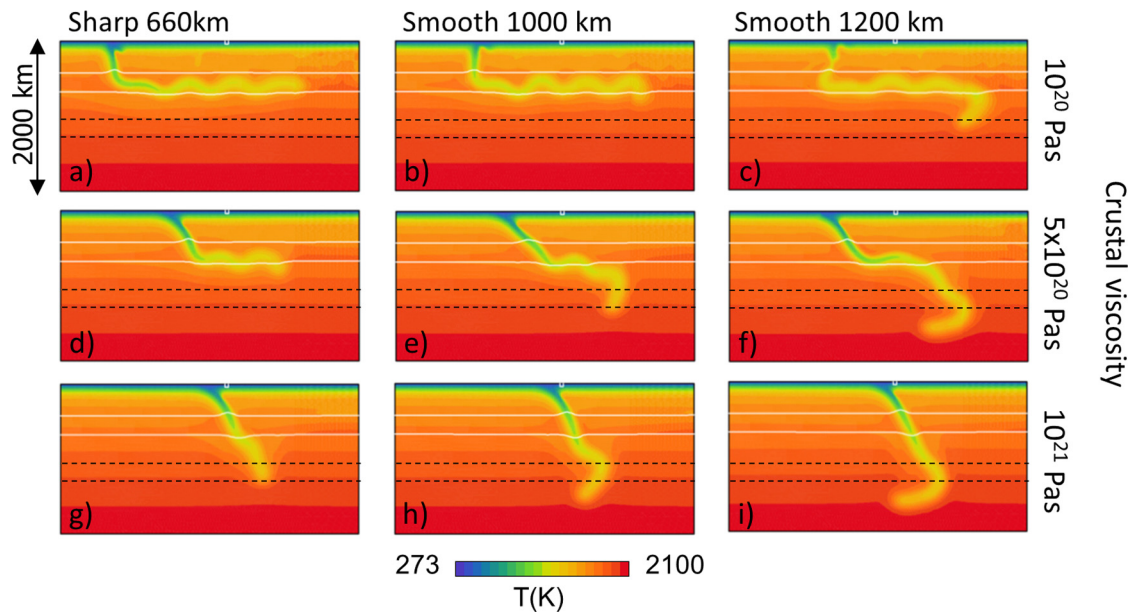


**Fig. 3.** Temperature snapshot taken at 80 Myr showing part of the model domain 2000 km deep and 4000 km wide. White square marks initial position of the trench; white lines indicate positions of the major phase transitions at 410 and 660-km; dashed black lines indicate the depths of 1000 km and 1200 km. All models shown here have 100 Myr old plate and regular phase transitions ( $\gamma_{410} = 2$ ,  $\gamma_{660} = -2.5$  MPa/K). Panels a)–c) show effect of viscosity interface between the upper and lower mantle in models with weakest crust. Panels d)–f) show models with intermediate crust. Panels g)–i) show models with strong crust.

regular phase transitions, and we discuss the effects of the upper-lower mantle viscosity interface and crustal viscosity. Each model is represented by one snapshot taken after 80 Myr of subduction evolution. Panels a–c represent models with a weak crust. As already discussed above, the model SH660 (Fig. 3a) results in subhorizontal buckling and stagnation, and a similar deformation scenario is observed if we shift the viscosity interface deeper (SM1000, Fig. 3b). In case of yet deeper rheological layering (SM1200, Fig. 3c) the tip initially penetrates to 1200 km depth, where it encounters the stiff material, and again rollback is initiated. The slab tips in the models with a deeper rheological boundary (SM1000 and SM1200) are thus embedded in the shallow lower mantle while the rest of the subducted slab lies flat above the phase boundary at 660-km depth. The maximum tip depth thus depends on the depth of the rheological layering; later, however, all three models with weak crust exhibit rollback and deform subhorizontally until the crust is consumed and break-off follows. After slab detachment, horizontally buckled flat-lying slabs in models SH660 and SM1000 remain stagnant around the phase boundary at 660 km depth and only very slowly sink into the lower mantle, with sinking speed of the order of 0.1 cm/yr (Fig. 5). On the other hand, in model SM1200 a deeper slab tip (Fig. 3c) produces enough pull to make detached-slab sinking more efficient, and sinking velocity thus increases to  $\sim 0.5$  cm/yr (Fig. 5, orange dotted line).

When the decoupling crustal layer has intermediate strength ( $\eta_{cr} = 5 \times 10^{20}$  Pas), the effects of the viscosity changeover between the upper and lower mantle on slab deformation and stagnation become more evident. Fig. 3d–f shows the three viscosity models (SH660, SM1000 and SM1200) with 100 Myr-old plate and regular phase transitions. Intermediate-crust results thus can be compared to the corresponding weak-crust models (Fig. 3a–c). With intermediate crust, only the sharp viscosity increase at 660 km depth is able to prevent slab penetration, and after 80 Myr we thus observe the slab horizontally buckled and lying flat above the 660-km interface (Fig. 3d). When the viscosity interface is shifted deeper, either to 1000 km or 1200 km (Fig. 3e–f), a significant amount of slab material initially penetrates into the lower mantle. Lower viscous resistance of the uppermost lower mantle results in higher subducting plate velocities ( $\sim 3$  cm/yr in model

SM1000, 5 cm/yr in model SM1200) compared to model SH660 ( $\sim 2$  cm/yr) and consequently in reduction of the rollback. Though the slab later rolls back, its trench retreat is less efficient, and the slab is simultaneously sinking into the lower mantle. In case of model SM1000, part of the flat-lying segment remains temporarily stable below the 660-km phase boundary and above 1000 km depth.

Increasing the strength of the decoupling crustal layer yet more, to  $\eta_{cr} = 10^{21}$  Pas (Fig. 3g–i), results in further reduction of subduction and plate velocities. Stiff contact of the plates causes rotation of the subducting slab towards vertical which reduces rollback (Čížková and Bina, 2013), and slabs directly penetrate in all models regardless the structure of the viscosity transition between the upper and lower mantle.

### 3.2. Effect of phase transitions

In the above models we assumed regular major phase transitions. The effect of their strength, parameterized through their Clapeyron slopes, is further illustrated in Fig. 4. For this comparison we used a model with a weak crust and a smooth viscosity increase at 1000 km. Panel 4a is for the model without phase transitions; panel 4b has regular exothermic phase transition at 410 km ( $\gamma_{410} = 2$  MPa/K) and a weaker endothermic transition at 660 km ( $\gamma_{660} = -1.5$  MPa/K), and panel 4c has the regular transitions ( $\gamma_{410} = 2$  MPa/K,  $\gamma_{660} = -2.5$  MPa/K). As already mentioned above, regular phase transitions (Fig. 4c) result in horizontal buckling and long-term stagnation ( $\sim 200$  Myr) at 660 km depth after break-off. If both phase transitions are absent (Fig. 4a), the slab tip reaches the maximum depth of  $\sim 1000$  km. Due to the resistance of the high-viscosity lower mantle, the slab starts to roll back, and in the absence of phase transitions and associated weakening through stress-dependent rheology (Čížková and Bina, 2013), the trench is retreating quickly (4 cm/yr – 800 km within 20 Myr). The slab is sinking while rolling back, and after break-off it sinks through the lower mantle with a speed of  $\sim 0.9$  cm/yr, decelerating when approaching the bottom boundary (Fig. 5, green solid line). When the phase transitions are switched on, with a weaker endothermic transition at 660 km (Fig. 4b) the slab buckles and deforms

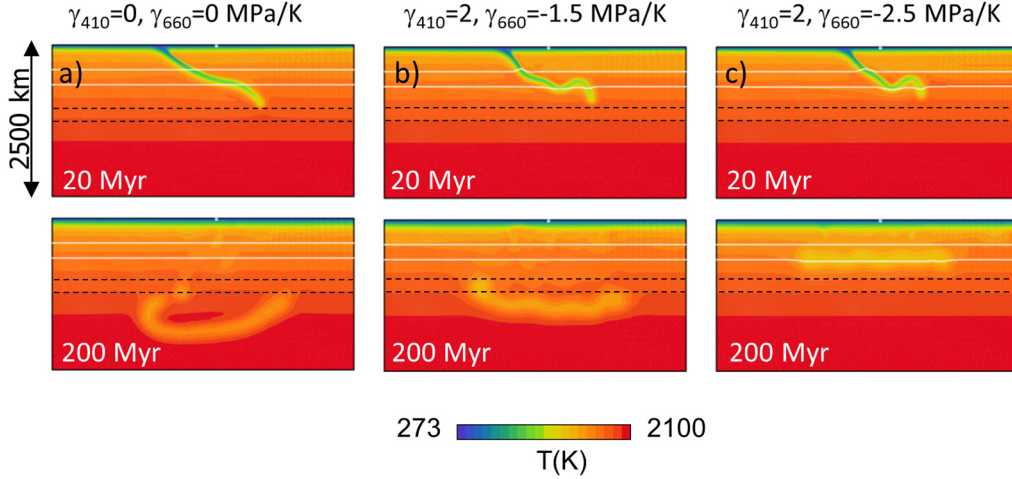


**Fig. 4.** The effect of phase transitions. Two snapshots showing part of the model domain 2500 km deep and 5000 km wide are centered around subduction. White squares mark initial position of the trench; white lines indicate positions of the major phase transitions at 410 and 660-km; dashed black lines indicate the depths of 1000 km and 1200 km. All models shown here have 100 Myr old plate and weak crust ( $\eta_{\text{crust}} = 10^{20}$  Pa s). Panel a) shows model without phase transitions; b) model with weaker endothermic phase transition at 660 km ( $\gamma_{410} = 2$ ,  $\gamma_{660} = -1.5$  MPa/K); c) model with regular phase transitions ( $\gamma_{410} = 2$ ,  $\gamma_{660} = -2.5$  MPa/K).

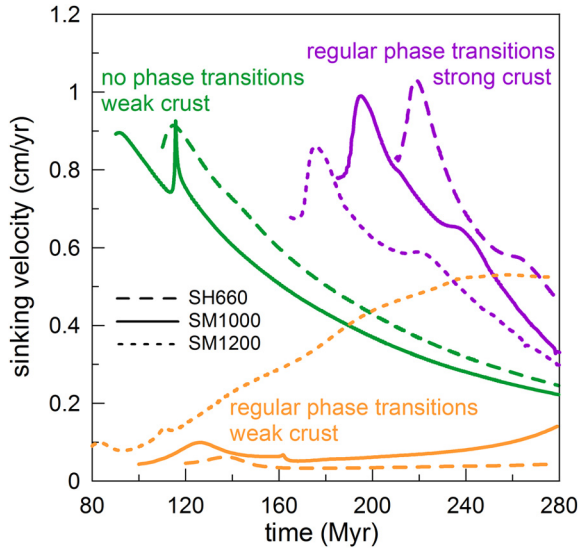


**Fig. 5.** Sinking velocity of the detached slab plotted from the moment of break-off as a function of time for the models with 100 Myr old subducting plate. Meaning of the symbols is as follows. Viscosity changeover between the upper and lower mantle: sharp at 660 km (dashed line), smooth at 1000 km (solid line), smooth at 1200 km (dotted line). Crustal viscosity:  $10^{20}$  Pa s (orange line),  $10^{21}$  Pa s (purple line). Regular phase transitions at 410-km and 660-km depths ( $\gamma_{410} = 2$  MPa/K,  $\gamma_{660} = -2.5$  MPa/K) are included in models plotted with orange and purple lines, green lines are for models without phase transitions.

very similarly to the regular case until the break-off moment. After slab detachment, however, the reduced strength of the 660-km phase transition results in more efficient sinking, and thus the slab remnant is at 200 Myr already half-way through the lower mantle, while in the case of a regular 660-km transition it is still stacked at the very top of the lower mantle (cf. Fig. 4b and 4c, lower panels).

### 3.3. Slab sinking after break-off

Different subduction modes as discussed in paragraph 3.1. result in different slab morphologies at the moment of break-off, and these inevitably affect free descent of detached slabs through the (lower) mantle. This later period of slab evolution is illustrated in Fig. 5, where sinking velocities of detached slabs are shown after the moment of break-off for selected models with 100 Myr old subducting plate. Sinking velocities are calculated as an av-

erage over the detached part of the slab. Models are apparently divisible into three groups. In models with strong crust and regular phase transitions (purple lines), at the moment of break-off the slab tips have already subducted deep into the lower mantle, and slabs are dipping relatively steeply. Detached slabs therefore continue in their descent, and they slow down when approaching the bottom of the model domain. Models with weak crust and regular phase transitions (orange lines) are at the moment of slab detachment lying flat (horizontally buckled) at the 660-km phase boundary. Since their negative thermal buoyancy is significantly compensated by the positive buoyancy associated with the endothermic phase boundary, they only very slowly sink, with a low sinking speed of about 1 mm/yr. The only exception is the model with a smooth viscosity increase at 1200 km depth (dotted orange line) that is accelerating due to the slab tip that initially managed to penetrate into the lower mantle as discussed above (Fig. 3c). This deeper tip is now efficiently pulling the whole detached slab. The third group of curves in the middle of the graph (green lines) shows models without phase transitions. In these models the slabs penetrated into the lower mantle (as in the absence of both phase transitions we do not observe horizontal buckling and stagnation), and thus they also sink immediately after break-off.

### 3.4. Stagnation versus penetration

To gain greater insight into whether the observed slab stagnation is transient or long-term in nature, we studied the temporal evolution of the slab penetration depth by embedding a suitable tracer within the body of the slab. Placing such a tracer within the leading tip of the slab is not informative, because the tip of the slab always initially penetrates. Stagnation does not occur until the leading portion of the slab begins to respond via coupling to the more viscous layer below, leading to rollback, buckling, and stagnation of an extended portion behind the tip (Čížková and Bina, 2013). Therefore, we placed a tracer  $\sim 600$  km behind the slab tip (white asterisk in Fig. 1c) and monitored its penetration depth as a function of time (Fig. 6). Models with weak crust (Fig. 6a) result in long-term stagnation above the endothermic phase boundary at 660-km depth. Only the model SM1200 (green line), where the leading tip that initially penetrated to  $\sim 1200$  km pulls the stagnant slab, results in penetration after slab break-off at  $\sim 80$  Myr. Models with stiff crust (Fig. 6c), on the other hand, result in penetration regardless the viscosity stratification. In the case of models with intermediate crustal viscosity, it is evident that stagnation

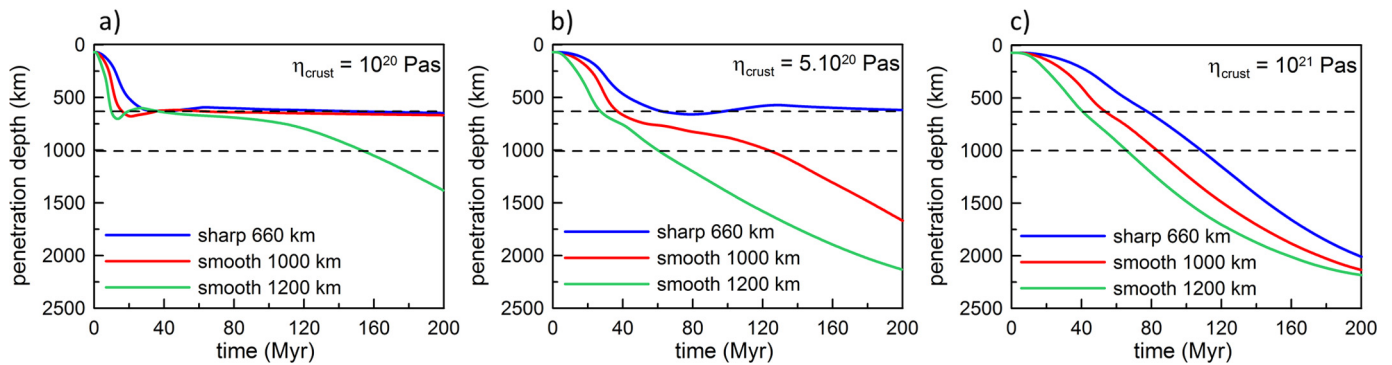


Fig. 6. Slab penetration depth monitored by a tracer placed initially 600 km behind the slab tip (white asterisk in Fig. 1c).

behavior exhibits significant dependence upon detailed viscosity structure (Fig. 6b). The central body of the slab either stagnates at the base of the upper mantle (sharp 660 km – blue line), temporarily stagnates between 660 km and 1000 km (smooth 1000 km – red line) or penetrates relatively quickly (smooth 1200 km – green line).

In order to better understand the forces that control slab stagnation or penetration, we further show the time evolution of density anomalies in the three models (SH660, SM1000, SM1200) with an intermediate crustal viscosity (Fig. 7). In these models the upper-lower mantle viscosity transition affects the ability to penetrate to the lower mantle (cf. Fig. 6b). In the model case with a sharp viscosity increase at 660 km (Fig. 7a), where the slab rolls back and deflects subhorizontally, the petrologically positively buoyant material associated with the thermally depressed endothermic phase change of ringwoodite to bridgmanite and ferropericlasite (red anomaly) stretches over the whole length of the flattened slab and thus efficiently compensates the negative buoyancy arising from its positive thermally induced density anomaly. The stagnant slab is warming up, and this thermal assimilation reduces both its negative thermal buoyancy and its positive petrological buoyancy while the slab is very slowly sinking through the phase boundary (with sinking velocity  $\sim 0.1$  cm/yr). In the models with the rheological transition at 1000-km depth (Fig. 7b) we have a negatively buoyant tip that initially penetrates to the lower mantle and pulls the slab, and at the same time the lateral extent of the flat-lying portion of the slab at the 660-km interface is limited – therefore the net negative buoyancy anomaly of the slab is stronger than in the model SH660 and the slab penetrates to the lower mantle after a temporary stagnation period. Yet deeper rheological transition between the upper and lower mantle (SM1200, Fig. 7c) results in a more deeply penetrated tip and even more greatly reduced lateral extent of the stagnant part of the slab, which reinforces penetration and further increases the sinking velocity ( $\sim 0.6$  cm/yr). Thus, the variation in penetration-vs-stagnation behavior in these cases is more strongly governed by differences in the lateral extent of flat-lying slab material atop the thermally depressed phase boundary (itself determined by extent of initial slab-tip penetration and prior slab rollback) than by any differences in absolute slab temperature at the boundary.

All model runs with regular phase transitions are summarized in a regime diagram in Fig. 8. This shows the maximum penetration depth of the slab as a function of trench retreat (distance of the trench from its initial position). Retreat in both Fig. 8a and 8b is measured at subduction cessation – the moment when subduction is locked because all decoupling crust has been consumed. After that moment the trench no longer retreats. Penetration depth in Fig. 8a is measured also at the moment when subduction stops. In Fig. 8b the penetration is measured at 280 Myr. The difference in penetration depths between panels 8a and 8b thus illustrates free sinking of the detached slab. Models nicely separate into three

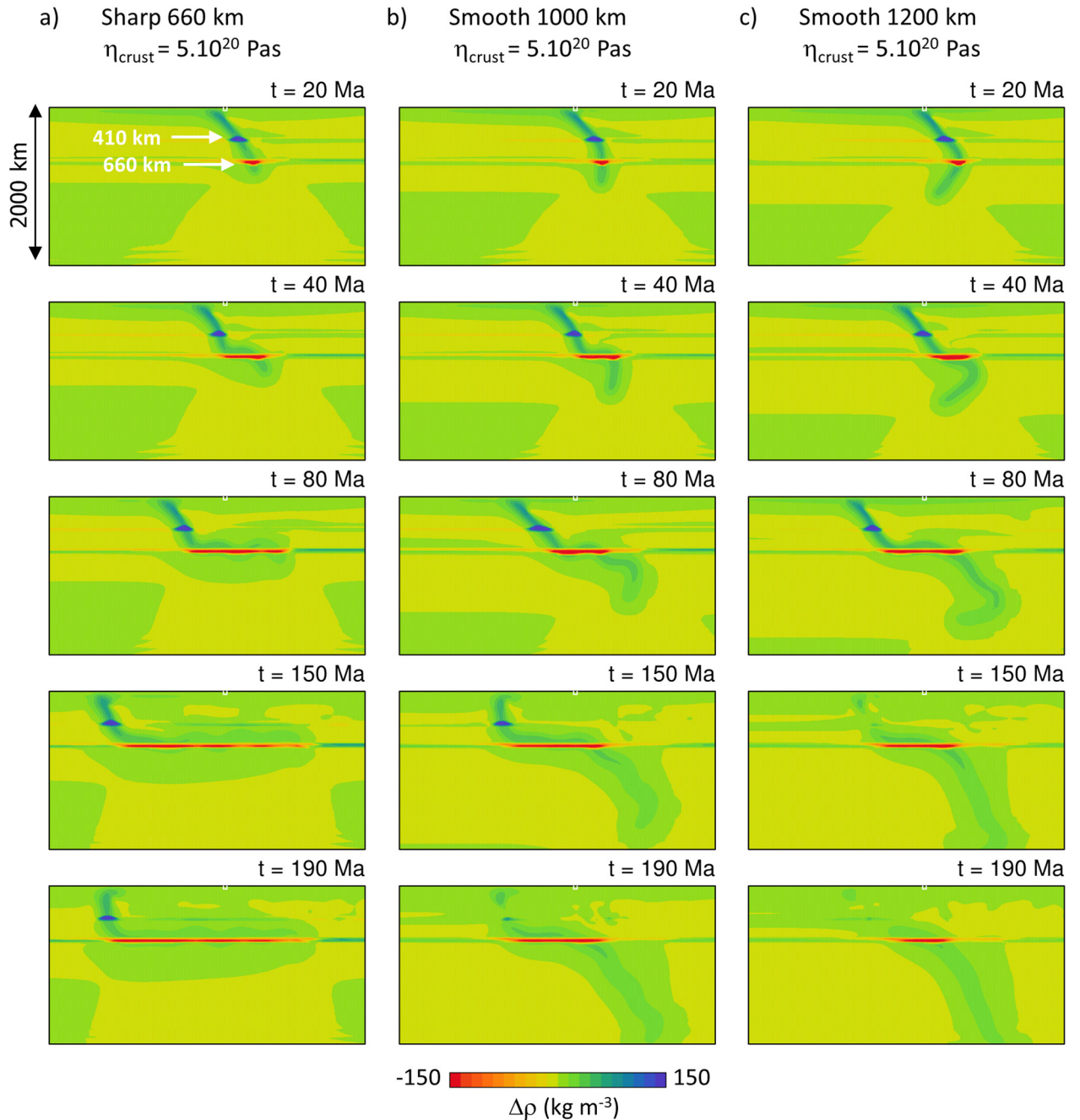
groups. In the first group are models with stiff crust (marked by yellow ellipse). Slabs in these models penetrate to the lower mantle without much resistance, and thus their tips are at about 2000 km depth at the moment of subduction cessation (Fig. 8a). Then they slowly sink to the base of the mantle (cf. panels 8a and 8b). In the second group are the models with weak crust (gray ellipse) that stagnate around 660 km depth. Retreat of these models reflects the length of the slab flattened above the 660-km interface. After break-off the slabs in this group sink only very slowly. Therefore the gray ellipse remains at rather shallow depths even at 280 Myr (Fig. 8b). The only exception to this second group is the model with both a weak crust and a deep viscosity increase at 1200 km (small light-blue half-open circle, marked in Fig. 8b also by dashed black arrow). In this model, the slab tip first penetrates into the lower mantle to  $\sim 1100$  km depth, and then the slab starts to roll back and buckle horizontally. After detachment, the sunken tip is heavy enough to pull the horizontally lying part of the slab into the lower mantle, and that is why in Fig. 8b we find this small half-open circle in the group of slabs that are in penetrative mode. In the third group are the models with intermediate crust (dark gray band) that show clear dependence on the nature of the viscosity transition between the upper and lower mantle. While the model with a sharp increase at 660 km (medium open light-blue circle) remains in the gray ellipse of models stagnant around the 660-km phase transition, the two models with viscosity boundaries shifted to 1000 km and 1200 km (medium light-blue circles: solid and half-open) develop a penetrating tip and later sink to the bottom of the mantle.

Fig. 8 demonstrates also the effects of plate age – results are shown for a reference 100 Myr-old plate (light-blue symbols), a younger plate of 50 Myr (red symbols) and an older plate of 150 Myr (dark-blue). It comes as no surprise that the younger plates systematically exhibit less trench retreat than the older and heavier plates. For subducting plates of every age we note that models with a deeper viscosity increase result in deeper penetration than models with a viscosity increase at 660-km depth (cf. corresponding solid/half-open and open symbols in Fig. 8a), due to easier initial penetration of the slab tip. Total trench retreat, on the other hand, is systematically higher in models with a sharp viscosity increase at 660 km compared to deeper and smoothed viscosity layering, as there is a trade-off between rollback and penetration – more penetration implying less rollback and vice versa. This trade-off is demonstrated by the clear division between the groups of retreating (gray ellipse in the upper right corner of diagram in Fig. 8b) and stagnating (yellow ellipse in lower left corner) slab models.

### 3.5. Effects of initial temperature distribution

Finally, let us briefly look at the effect of the initial temperature distribution. As pointed out above, in the models where an





**Fig. 7.** Time evolution of the density anomalies in the models with 100 Myr old plate and intermediate crustal viscosity  $\eta_{\text{crust}} = 5 \cdot 10^{20}$  Pas. Part of the model domain, 2000 km deep and 4000 km wide is shown. Density anomalies are calculated with respect to the reference mantle adiabat. White arrows indicate the position of the petrological density anomalies associated with the exothermic phase transition at 410-km depth and the endothermic phase transition at 660-km depth. a) model SH660, b) model SM1000, c) model SM1200.

increase of viscosity occurs deeper than at 660-km depth, the slab tip initially penetrates to the lower mantle and is embedded in the more viscous material at the depth of 1000 km (SM1000) or 1200 km (SM1200). This leading tip may then later pull the horizontally buckled part of the stagnant slab and thus significantly affect the time scales of stagnation/penetration. The penetration of the slab tip as it first encounters the upper-lower mantle boundary may however be affected by the initial temperature distribution, where the geometry (dip angle) of the tip is the result of a kinematic preliminary run. We therefore tested also another group of models that are initiated from another initial temperature distribution *Ini2* with a lower dip angle of the initial slab tip (Fig. 1d). For this initial model *Ini2* we repeated the calculations in the models

with 100 Myr old plate and regular phase transitions. The results for three mantle viscosity profiles and three crustal viscosities are summarized in Fig. 9. If we compare these results with the previous results for initial temperatures *Ini1* (cf. Fig. 3), we may conclude that the trends of slab behavior in response to the crustal viscosity and mantle viscosity stratification as discussed above are observed also for initial model *Ini2*. The slab morphology on the other hand may be somewhat different, and in the case of a sharp 660 km viscosity interface and intermediate crustal viscosity the slab now penetrates, while model *Ini1* resulted in stagnating mode. This only confirms that we are close to a threshold here, and any small change of parameters may shift the boundary between stagnation and penetration.



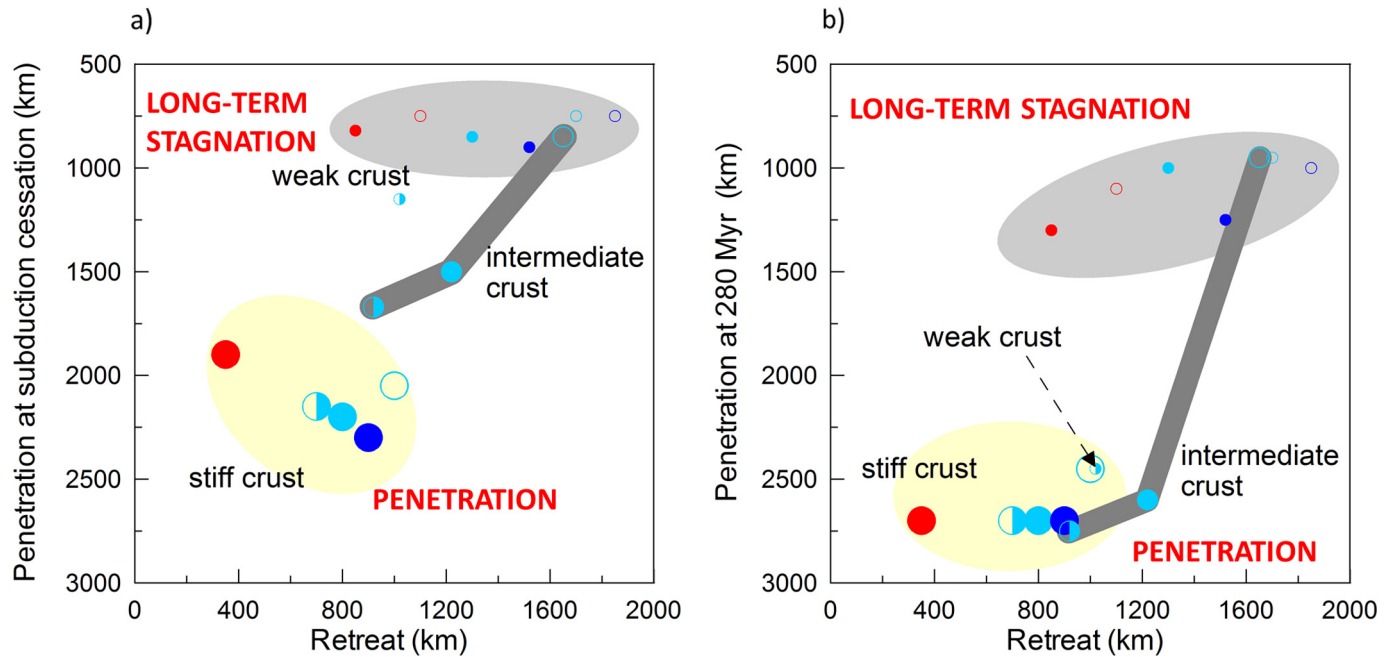


**Fig. 8.** Maximum penetration depth as a function of trench retreat for models with regular phase transitions. Meaning of the symbols is as follows. Plate age: 50 Myr (red), 100 Myr (light blue), 150 Myr (dark blue). Viscosity changeover between the upper and lower mantle: sharp at 660 km (open symbols), smooth at 1000 km (solid symbols), smooth at 1200 km (half-open symbols). Crustal viscosity:  $10^{20}$  Pa s (small symbols),  $5 \times 10^{20}$  Pa s (intermediate symbols),  $10^{21}$  Pa s (large symbols). Panel a) shows the situation at the moment when subduction stops; panel b) at 280 Myr, when all model slabs are detached and freely sinking through the mantle. Dashed arrow points to the only model with a weak crust that penetrated to the deep mantle (SM1200).

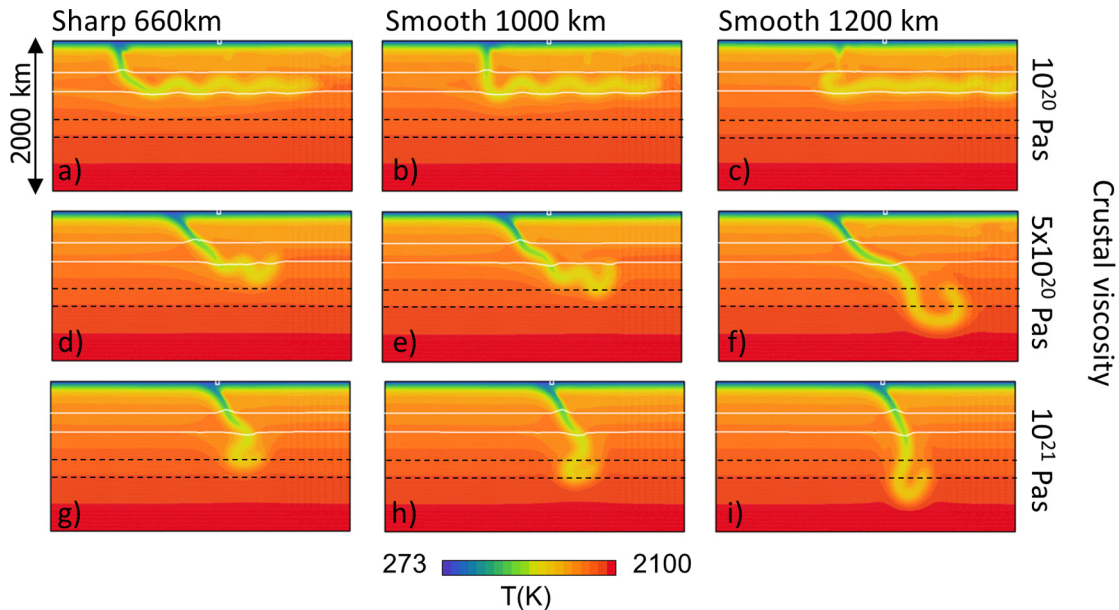


**Fig. 9.** The same as Fig. 3, but for the model with initial temperature distribution *Ini2* (Fig. 1d).

#### 4. Discussion and conclusions

Slab stagnation at the bottom of the transition zone is closely related to trench migration – retreating slabs tend to flatten above the 660-km interface, while non-retreating slabs penetrate to the lower mantle (e.g. Christensen, 1996; Čížková et al., 2002; Torii and Yoshioka, 2007; Agrusta et al., 2017). As previously shown, one of the factors that affects trench-retreat rate in free subduction models is the strength of the crustal shear zone that decouples the subducting and overriding plates. Weak crust favors rollback and stagnation while stiff decoupling crust reduces rollback and allows for slab penetration to the lower mantle in models with

sharp viscosity increase at 660-km depth (Čížková and Bina, 2013; Arredondo and Billen, 2017; Goes et al., 2017).

Here we tested crustal viscosities ranging between  $10^{20}$  Pa s and  $10^{21}$  Pa s. Weak crust ( $10^{20}$  Pa s) resulted in stagnant slabs trapped at the bottom of the transition zone. Strong crust ( $10^{21}$  Pa s) produced slabs that entered the lower mantle without much hindrance and continued their descent through the lower mantle. As the initial motivation for this study was slab stagnation in the shallow lower mantle, the most interesting results arise from models with intermediate crustal viscosity ( $5 \times 10^{20}$  Pa s). These show that, if a sharp viscosity interface is present at 660 km, the slab buckles horizontally above 660 km, but if the viscosity in-

interface is deeper, then a flat-lying part of the slab is able to sink into the lower mantle where we observe it to be temporarily stagnant between 660-km and 1000-km depths in agreement with recent tomographic indications (Fukao and Obayashi, 2013).

The nature of the viscosity interface between the upper and lower mantle (sharp vs. smooth, and localized at the phase boundary vs. shifted deeper) plays only a secondary role. However, in the case of intermediate crustal viscosity, slab dynamics are close to a threshold between penetrative (slow rollback) mode and stagnating (fast rollback) mode. In this case, the character of the viscosity transition between the upper and lower mantle selects for slab penetration or stagnation.

Alternatively, looking at the above results from another perspective, one may conclude that for a given upper-lower mantle viscosity transition the crustal viscosity controls the slab penetration. Then the rheological model with a viscosity increase located at 1000 km depth is able to explain slab stagnation in the upper mantle above the 660-km depth observed in some subduction zones as well as the slabs stagnant between 660-km and 1000-km depths reported in seismic tomography elsewhere. The crustal strength is then the factor that selects the mode of subduction deformation around the upper-lower mantle boundary.

A weak crustal layer is often assumed to be simply a numerical modeling convenience that allows decoupling of the plates. The weak lubricating layer, however, has genuine petrological bases, though using a 10-km thick layer with constant properties is certainly an oversimplification. In nature such lubrication may be provided and controlled by a variety of factors, whose relative impact may vary between subduction zones. Serpentinization weakening of mafic crust and of ultramafic lithospheric mantle (Hilairet et al., 2007; Amiguet et al., 2012; Guillot et al., 2015) may play a major role, where the depths of serpentine transformation and dehydration are thermally controlled (by plate age, convergence rate, and dip angle) and serpentinization by hydrothermal circulation through outer-rise faults is controlled by plate age (temperature), bending (dip angle), and seamount emplacement (porosity) (Ivandić et al., 2010; Hatakeyama et al., 2017). The extent of subduction of continental and oceanic sediments also may play a significant role, where sediment transport by processes of subduction erosion vary with rate of sediment supply, convergence rate, plate bending (dip angle), and subduction of buoyant features (e.g., seamounts, ridges) (Stern, 2011). Furthermore, depths of interplate decoupling and brittle-ductile transition depend on the ages of subducting and overriding plates (Arcay, 2012). The presence of blueschist-facies metamorphic assemblages in the subduction complex provide another avenue for control of crustal deformation by temperature, via dehydration embrittlement of glaucophane (vs. lawsonite) (Kim et al., 2015) and transition of lawsonite-blueschist to eclogite (Cao and Jung, 2016). Pursuing such details in the rheological approximation of the decoupling crustal layer is far beyond the scope of this work, but this weak layer may thus be viewed as a kind of proxy for the effects that may control rollback efficiency and trench migration rates, such as dehydration-related weakening and extension of the overriding plate (Nakao et al., 2018).

Schellart et al. (2011) have reported subducting plate velocities of the order of 4.2 cm/yr and relatively low trench velocities of  $\sim 1.7$  cm/yr in the center of wide natural subduction zones. Model SH660 with 100 Myr old subducting plate yields the reverse partitioning between plate and rollback velocities with rollback almost twice as fast as plate velocity (cf. Fig. 2b). Reduction of the rollback velocities was recently observed by Holt and Becker (2017) in models with power-law mantle rheology. Our results show that shifting the rheological transition to 1000 km further increases subducting plate velocities with respect to rollback velocities. The ratio between plate and rollback velocities almost doubles between the case of model SH660 with 100 Myr old plate and weak crust

and the case of corresponding model SM1000, and it nearly triples for model SM1000 with a younger (50 Myr old) subducting plate, approaching values reported by Schellart et al. (2011).

Sinking speed of detached slab segments in the lower mantle varies between 1 cm/yr in the models with slow rollback and penetrating slabs and 1 mm/yr in the models characterized by fast rollback and horizontal stagnation at the base of the transition zone. This is rather low compared to the value of 1–2 cm/yr derived from the correlation between subducted slab signatures in seismic tomography and the geological record (van der Meer et al., 2010, 2018). Since we focus on slab stagnation here, we use a specific model setup that allows unhindered rollback (free mobile ridge on the RHS of the overriding plate) which favors slab horizontal deformation and stagnation. Flattened slabs sink more slowly than vertically dipping slabs, and the very low sinking rates ( $\sim 1$  mm/yr) are further reinforced by the petrological buoyancy associated with the 660-km phase transition.

Furthermore, we looked more deeply into the effects of phase transitions. We adopt a phase-function parameterization of their buoyancy and latent heat effects (Christensen and Yuen, 1985) with prescribed Clapeyron slopes and density contrasts. In modeling studies, olivine composition is often used with corresponding phase transition parameters. However, since these have been shown to exaggerate the phase transition effects acting in a pyrolytic mantle (Arredondo and Billen, 2016), here we use a reduced value of Clapeyron slope of the olivine-wadsleyite transition, and in the case of the endothermic transition at 660-km depth which has presumably a more pronounced effect on the penetration, we test three values ranging between 0 and  $-2.5$  MPa/K in order to assess sensitivity to this parameter. We conclude that if the phase transitions are switched off, then slabs roll back due to the viscosity increase, but simultaneously they penetrate into the lower mantle. An endothermic phase transition at 660 km is thus crucial for generating horizontally deflected stagnant slabs at the bottom of the transition zone. The effective Clapeyron slope required for transition zone stagnation may, however, be smaller in magnitude than the value of  $-2.5$  MPa/K traditionally used for the ringwoodite to bridgmanite-plus-ferropericlasite transition.

The positive buoyancy associated with the 660-km phase transition is not the only effect that hampers slab penetration. Viscosity increase in the lower mantle forms another barrier to slab descent (e.g. Christensen, 1996; Olbertz et al., 1997; Garel et al., 2014) and in some studies was even identified as a primary reason for slab stagnation (Torii and Yoshioka, 2007; Yoshioka and Naganoda, 2010; Yoshida, 2014). In kinematically driven models with pressure- and temperature-dependent viscosity (Torii and Yoshioka, 2007; Yoshioka and Naganoda, 2010) a viscosity contrast higher than 10–30 ensures slab stagnation regardless of the Clapeyron slope of the 660-km phase transition. Our rheological description assumes a nonlinear composite model based on wet olivine parameters in the upper mantle, while the lower mantle deforms via diffusion creep with parameters based on sinking speed analysis (Čížková et al., 2012). That results in about one order of magnitude viscosity contrast between the upper and lower mantle. In our free subduction model with nonlinear stress-dependent rheology, such a viscosity contrast is not sufficient to prevent penetration in the absence of an endothermic phase transition, and both factors are needed to secure slab stagnation (Goes et al., 2017).

The models presented here focus on the mutual interplay of two rheological factors – crustal viscosity that controls the subducting plate velocity as well as the rollback rate, and viscosity stratification at the boundary between the upper and lower mantle. Of course, many other factors that affect subduction behavior are clearly present in natural subduction zones. Application of our results to individual subduction zones may, therefore, po-

tentially be complicated by other effects, such as the presence of surrounding plates (Yamato et al., 2009), remotely forced mantle flow (Chertova et al., 2018) or properties of the overriding plate (Garel et al., 2014).

## Acknowledgements

We thank three anonymous reviewers for comments on the manuscript that helped to improve the text. We acknowledge support by the Grant Agency of Czech Republic under project number 18-20818S.

## References

- Agrusta, R., van Hunen, J., Goes, S., 2014. The effect of metastable pyroxene on the slab dynamics. *Geophys. Res. Lett.* 41, 8800–8808.
- Agrusta, R., Goes, S., van Hunen, J., 2017. Subducting-slab transition zone interaction: stagnation, penetration and mode switches. *Earth Planet. Sci. Lett.* 464, 10–23. <https://doi.org/10.1016/j.epsl.2017.02.005>.
- Amiguet, E., Reynard, B., Caracas, R., Van de Moortèle, B., Hilaret, N., Wang, Y., 2012. Creep of phyllosilicates at the onset of plate tectonics. *Earth Planet. Sci. Lett.* 345–348, 142–150.
- Arcay, D., 2012. Dynamics of interplate domain in subduction zones: influence of rheological parameters and subducting plate age. *Solid Earth* 3, 467–488. <https://doi.org/10.5194/se-3-467-2012>.
- Arredondo, K.M., Billen, M.I., 2016. The effects of phase transitions and compositional layering in two-dimensional kinematic models of subduction. *J. Geodyn.* 100, 159–174. <https://doi.org/10.1016/j.jog.2016.05.009>.
- Arredondo, K.M., Billen, M.I., 2017. Coupled effects of phase transitions and rheology in 2D dynamical models of subduction. *J. Geophys. Res., Solid Earth* 122, 5813–5830. <https://doi.org/10.1002/2017JB014374>.
- Ballmer, M., Schmerr, N.C., Nakagawa, T., Ritsema, J., 2015. Compositional mantle layering revealed by slab stagnation at ~1000-km depth. *Sci. Adv.* 1, e1500815.
- Běhouňková, M., Čížková, H., 2008. Long-wavelength character of subducted slabs in the lower mantle. *Earth Planet. Sci. Lett.* 275, 43–53.
- Billen, M., 2008. Modeling the dynamics of subducting slabs. *Annu. Rev. Earth Planet. Sci.* 36, 325–356.
- Bina, C.R., Helffrich, G., 1994. Phase-transition Clapeyron slopes and transition zone seismic discontinuity topography. *J. Geophys. Res.* 99, 15853–15860.
- Bina, C.R., Kawakatsu, H., 2010. Buoyancy, bending, and seismic visibility in deep slab stagnation. *Phys. Earth Planet. Inter.* 183, 330–340.
- Bina, C.R., Stein, S., Marton, F.C., Van Ark, E.M., 2001. Implications of slab mineralogy for subduction dynamics. *Phys. Earth Planet. Inter.* 127, 51–66.
- Bolfan-Casanova, N., Keppler, H., Rubie, D.C., 2003. Water partitioning at 660 km depth and evidence for very low water solubility in magnesium silicate perovskite. *Geophys. Res. Lett.* 30, 1905.
- Cao, Y., Jung, H., 2016. Seismic properties of subducting oceanic crust: constraints from natural lawsonite-bearing blueschist and eclogite in Sivrihisar Massif, Turkey. *Phys. Earth Planet. Inter.* 250, 12–30. <https://doi.org/10.1016/j.pepi.2015.10.003>.
- Chen, J., Weidner, D.J., Vaughan, M.T., 2002. The strength of Mg<sub>0.9</sub>Fe<sub>0.1</sub>SiO<sub>3</sub> perovskite at high pressure and temperature. *Nature* 419, 824–826.
- Chertova, M., Spakman, W., Steinberger, B., 2018. Mantle flow influence on subduction evolution. *Earth Planet. Sci. Lett.* 489, 258–266.
- Chopelas, A., Boehler, R., 1992. Thermal expansivity in the lower mantle. *Geophys. Res. Lett.* 19, 1983–1986.
- Christensen, U.R., 1996. The influence of trench migration on slab penetration into the lower mantle. *Earth Planet. Sci. Lett.* 140, 27–39. [https://doi.org/10.1016/0012-821X\(96\)00023-4](https://doi.org/10.1016/0012-821X(96)00023-4).
- Christensen, U.R., 2001. Geodynamic models of deep subduction. *Phys. Earth Planet. Inter.* 127, 25–34.
- Christensen, U.R., Yuen, D.A., 1984. The interaction of a subducting lithospheric slab with a chemical or phase boundary. *J. Geophys. Res.* 89, 4389–4402.
- Christensen, U.R., Yuen, D.A., 1985. Layered convection induced by phase transitions. *J. Geophys. Res.* 90, 10,291–10,300. <https://doi.org/10.1029/JB090iB12p10291>.
- Čížková, H., Bina, C.R., 2013. Effects of mantle and subduction-interface rheologies on slab stagnation and trench rollback. *Earth Planet. Sci. Lett.* 379, 95–103. <https://doi.org/10.1016/j.epsl.2013.08.011>.
- Čížková, H., van Hunen, J., van der Berg, A.P., Vlaar, N.J., 2002. The influence of rheological weakening and yield stress on the interaction of slabs with the 670 km discontinuity. *Earth Planet. Sci. Lett.* 199, 447–457. [https://doi.org/10.1016/S0012-821X\(02\)00586-1](https://doi.org/10.1016/S0012-821X(02)00586-1).
- Čížková, H., Čadež, O., Yuen, D.A., Zhou, H., 1996. Slope of the geoid spectrum and constraints on mantle viscosity stratification. *Geophys. Res. Lett.* 23, 3063–3066.
- Čížková, H., van Hunen, J., van den Berg, A.P., 2007. Stress distribution within subducting slabs and their deformation in the transition zone. *Phys. Earth Planet. Inter.* 161, 202–214.
- Čížková, H., van den Berg, A.P., Spakman, W., Matyska, C., 2012. The viscosity of Earth's lower mantle inferred from sinking speed of subducted lithosphere. *Phys. Earth Planet. Inter.* 200–201, 56–62.
- Faccenda, M., Dal Zilio, L., 2017. The role of solid-solid phase transitions in mantle convection. *Lithos* 268–271, 198–224. <https://doi.org/10.1016/j.lithos.2016.11.007>.
- French, S.W., Romanowicz, B., 2015. Broad plumes rooted at the base of the Earth's mantle beneath major hotspots. *Nature* 525, 95–99.
- Fukao, Y., Obayashi, M., Nakakuki, T., et al., 2009. Stagnant slab: a review. *Annu. Rev. Earth Planet. Sci.* 37, 19–46.
- Fukao, Y., Obayashi, M., 2013. Subducted slabs stagnant above, penetrating through, and trapped below the 660 km discontinuity. *J. Geophys. Res.* 118, 5920–5938.
- Garel, F., Goes, S., Davies, D.R., Davies, J.H., Kramer, S.C., Wilson, C.R., 2014. Interaction of subducted slabs with the mantle transition zone: a regime diagram from 2-D thermo-mechanical models with a mobile trench and an overriding plate. *Geochem. Geophys. Geosyst.* 15, 1739–1765. <https://doi.org/10.1002/2014GC005257>.
- Goes, S., Agrusta, R., van Hunen, J., Garel, F., 2017. Subduction-transition zone interactions: a review. *Geosphere* 13, 3. <https://doi.org/10.1130/GES01476.1>.
- Guillot, S., Schwartz, S., Reynard, B., Agard, P., Prigent, C., 2015. Tectonic significance of serpentinites. *Tectonophysics* 646, 1–19. <https://doi.org/10.1016/j.tecto.2015.01.020>.
- Hatakeyama, K., Katayama, I., Hirauchi, K., Michibayashi, K., 2017. Mantle hydration along outer-rise faults inferred from serpentinized permeability. *Sci. Rep.* 7, 13870. <https://doi.org/10.1038/s41598-017-14309-9>.
- Hilaret, N., Reynard, B., Wang, Y., Daniel, I., Merkel, S., Nishiyama, N., Petitgirard, S., 2007. High-pressure creep of serpentine, interseismic deformation, and initiation of subduction. *Science* 318, 1910–1913. <https://doi.org/10.1126/science.1148494>.
- Hirth, G., Kohlstedt, D., 2003. Rheology of the upper mantle and mantle wedge: a view from the experimentalists. In: *Inside the Subduction Factory*. In: *Geophys. Monogr.*, vol. 138. American Geophysical Union, Washington, DC.
- Holt, A.F., Becker, T.W., 2017. The effect of a power-law mantle viscosity on trench retreat rate. *Geophys. J. Int.* 208, 491–507. <https://doi.org/10.1093/gji/ggw392>.
- Ivancic, M., Grevenmeyer, I., Bialas, J., Petersen, C.J., 2010. Serpentinization in the trench-outer rise region offshore of Nicaragua: constraints from seismic refraction and wide-angle data. *Geophys. J. Int.* 180, 1253–1264. <https://doi.org/10.1111/j.1365-246X.2009.04474.x>.
- Katsura, T., Yokoshi, S., Kawabe, K., Shatskiy, A., Manthilake, M.A.G.M., Zhai, S., Fukui, H., Hegoda, H.A.C.I., Yoshino, T., Yamazaki, D., Matsuzaki, T., Yoneda, A., Ito, E., Sugita, M., Tomioka, N., Hagiya, K., Nozawa, A., Funakoshi, K., 2009. P–V–T relations of MgSiO<sub>3</sub> perovskite determined by in situ X-ray diffraction using a large-volume high-pressure apparatus. *Geophys. Res. Lett.* 36, L01305.
- Kim, D., Katayama, I., Wallis, S., Michibayashi, K., Miyake, A., Seto, Y., Azuma, S., 2015. Deformation microstructures of glaucophane and lawsonite in experimentally deformed blueschists: implications for intermediate-depth intraplate earthquakes. *J. Geophys. Res.* 120, 1229–1242.
- King, S.D., 2016. An evolving view of transition zone and midmantle viscosity. *Geochem. Geophys. Geosyst.* 17, 1234–1237.
- King, S.D., Frost, D.J., Rubie, D.C., 2015. Why cold slabs stagnate in the transition zone. *Geology* 43, 231–234.
- Liu, X., Zhong, S., 2016. Constraining mantle viscosity structure for a thermochemical mantle using the geoid observation. *Geochem. Geophys. Geosyst.* 17, 895–913.
- Marquardt, H., Miyagi, L., 2015. Slab stagnation in the shallow lower mantle linked to an increase in mantle viscosity. *Nat. Geosci.* 8, 311–314.
- Mitrovica, J.X., Forte, A.M., 1997. Radial profile of mantle viscosity: results from the joint inversion of convection and postglacial rebound observables. *J. Geophys. Res.* 102, 2751–2769.
- Nakao, A., Iwamori, H., Nakakuki, T., Suzuki, Y.J., Nakamura, H., 2018. Roles of hydrous lithospheric mantle in deep water transportation and subduction dynamics. *Geophys. Res. Lett.* 45. <https://doi.org/10.1029/2017GL076953>.
- Olbertz, D., Wortel, M.J.R., Hansen, U., 1997. Trench migration and subduction zone geometry. *Geophys. Res. Lett.* 24, 221–224. <https://doi.org/10.1029/96GL03971>.
- Rudolph, M.L., Lekic, V., Lithgow-Bertelloni, C., 2015. Viscosity jump in Earth's mid-mantle. *Science* 350, 1349.
- Schellart, W.P., Stegman, D.R., Farrington, R.J., Moresi, L., 2011. Influence of lateral slab edge distance on plate velocity, trench velocity, and subduction partitioning. *J. Geophys. Res.* 116, B10408. <https://doi.org/10.1029/2011JB008535>.
- Segal, A., Praagman, N., 2005. The SEPRAN FEM Package. Technical report. Delft Univ. Technol., Ingenieursbureau SEPRAN, The Netherlands. <http://ta.twi.tudelft.nl/sepran/sepran.html>.
- Steinbach, V., Yuen, D.A., 1995. The effects of temperature-dependent viscosity on mantle convection with the two major phase transitions. *Phys. Earth Planet. Inter.* 90, 13–36.
- Stern, C.R., 2011. Subduction erosion: rates, mechanisms, and its role in arc magmatism and the evolution of the continental crust and mantle. *Gondwana Res.* 20, 284–308. <https://doi.org/10.1016/j.jgr.2011.03.006>.
- Tetzlaff, M., Schmeling, H., 2000. The influence of olivine metastability on deep subduction of oceanic lithosphere. *Phys. Earth Planet. Inter.* 120, 29–38.



- Torii, Y., Yoshioka, S., 2007. Physical conditions producing slab stagnation: constraints of the Clapeyron slope, mantle viscosity, trench retreat, and dip angles. *Tectonophysics* 445, 200–209.
- van den Berg, A.P., van Keken, P.E., Yuen, D.A., 1993. The effects of a composite non-Newtonian and Newtonian rheology on mantle convection. *Geophys. J. Int.* 115, 62–78.
- van der Meer, D.G., Spakman, W., van Hinsbergen, D.J.J., Amaru, M.L., Torsvik, T.H., 2010. Towards absolute plate motions constrained by lower-mantle slab remnants. *Nat. Geosci.* 3, 36–40.
- van der Meer, D.G., van Hinsbergen, D.J.J., Spakman, W., 2018. Atlas of the under-world: slab remnants in the mantle, their sinking history, and a new outlook on lower mantle viscosity. *Tectonophysics* 723, 309–448.
- van Hunen, J., van den Berg, A.P., Vlaar, N.J., 2002. On the role of subducting oceanic plateaus in the development of shallow flat subduction. *Tectonophysics* 352, 317–333.
- Wood, B.J., Rubie, D.C., 1996. The effect of alumina on phase transformations at the 660-kilometer discontinuity from Fe–Mg partitioning experiments. *Science* 273, 1522–1524.
- Yamato, P., Husson, L., Braun, J., Loiselet, C., Thieulot, C., 2009. Influence of surrounding plates on 3D subduction dynamics. *Geophys. Res. Lett.* 36, L07303. <https://doi.org/10.1029/2008GL036942>.
- Yamazaki, D., Karato, S., 2001. Some mineral physics constraints on the rheology and geothermal structure of Earth's lower mantle. *Am. Mineral.* 86, 385–391.
- Yoshida, M., 2014. A new conceptual model for whole mantle convection and the origin of hotspot plumes. *J. Geodyn.* 78, 32–41. <https://doi.org/10.1016/j.jog.2014.04.004>.
- Yoshioka, S., Naganoda, A., 2010. Effects of trench migration on fall of stagnant slabs into the lower mantle. *Phys. Earth Planet. Inter.* 183, 321–329. <https://doi.org/10.1016/j.pepi.2010.09.002>.